

Unravelling Charge Storage Mechanisms of Lithium, Sodium and Potassium into Graphene-Coffee Waste Derived Hard Carbon Composites

Juan Luis Gómez-Urbano,^[a, b, c] Christian Leibing,^[c] María Jauregui,^[a]
Sandesh Darlami-Magar,^[c] Damien Saurel,^[a] Daniel Carriazo,^{*[a, d]} and Andrea Balducci^{*[c]}

Hard carbons are promising anode materials for lithium, sodium and potassium-ion batteries attending to their low cost, simple processing technology and outstanding electrochemical performance. However, their complex structure and controversial carrier-ion storage mechanisms makes difficult the prediction of their performance. Herein, we investigate the insertion storage mechanisms behind of three different alkali metal ions (lithium, sodium and potassium) into a hard carbon composite obtained by the pyrolysis of coffee waste and graphene oxide. The insertion/deinsertion processes have been monitored by galva-

nostatic intermittent titration technique and *operando* X-Ray diffraction. Results reveal that alkaline metal ions follow an adsorption-intercalation mechanism where the high potential region can be ascribed to the adsorption of the alkaline metal ions on the surface active sites, while slopping region arises from their intercalation between the pseudo-graphitic micro-crystallites. Moreover, the graphene-coffee waste hard carbon exhibits a notorious capacity retention after 300 charge/discharge cycles in all the alkaline metals evaluated.

Introduction

Since 1991, when Sony commercialized the first lithium-ion battery (LiBs), they have been the preferred energy storage technology in portable electronics and cordless devices. LiBs show higher energy density, higher voltage and lower self-discharge compared to other energy storage systems thanks to the intrinsic features of lithium ions. However, great concerns have raised over the use of critical raw materials (Li, Co, Ni, Cu or graphite) in terms of affordability and cost due to its scarcity and unevenly distributed resources in the Earth's crust. On this regard, sodium-ion batteries (SiBs) and potassium-ion batteries (KiBs) have attracted great interest as alternatives to LiBs. Sodium and potassium are the sixth and seventh most abundant elements in the Earth's crust^[1] and are widely and

homogeneously distributed, ensuring a sustainable, low cost and stable growth of large energy storage system market.^[2] Moreover, moving to these technologies allow replacing Cu anode foil by Al foil, which considerably decreases the total cost of the cells.^[3] The energy output of alkaline metal-ion batteries is greatly influenced by the composition and structure of both positive and negative electrodes. On the cathode side, encouraging performances have been achieved either for SiBs and KiBs through the development of novel layered metal oxides,^[4,5] polyanionic compounds,^[6,7] or organic materials.^[8,9] Nevertheless, further improvements are needed in the anode side to achieve the maximum potential of these devices. Commercial graphite, being the preferred choice for LiBs, have been widely explored for their use in Na and K batteries. However, very low specific capacity (ca. 35 mAh g⁻¹) is measured for SiBs in most of the conventional organic electrolytes.^[10] This was first attributed to the larger ionic radius of Na (1.02 Å) over Li (0.76 Å), but recent studies demonstrated that this poor behavior is a consequence of the low binding energy between graphite and Na.^[11,12] In contrast to sodium, potassium can be successfully intercalated in graphite to form stable compounds (GICs), reaching reversible specific capacity of ca. 279 mAh g⁻¹.^[13] However, cycle life and capacity retention of KiBs are strongly penalized due to the large volume expansion undergone upon the intercalation of K (1.38 Å). Several candidates have been proposed as alternatives to graphite, such as alloy-type materials,^[14] sulfides^[15] or MXenes.^[16] Unfortunately, even when high specific capacities are achieved, most of them are very expensive or require complex synthetic procedures, which limit their practical application for grid-scale energy storage applications. Besides graphite, carbonaceous materials are up to date considered the most promising host materials for SiBs and KiBs due to their low price and high

[a] J. L. Gómez-Urbano, M. Jauregui, D. Saurel, D. Carriazo
CIC EnergíGUNE
Parque Tecnológico de Álava, 01510 Miñano, Álava (Spain)
E-mail: dcarriazo@cicenergigune.com

[b] J. L. Gómez-Urbano
Universidad Del País Vasco UPV/EHU
48080 Bilbao (Spain)

[c] J. L. Gómez-Urbano, C. Leibing, S. Darlami-Magar, Prof. A. Balducci
Institute for Technical Chemistry and Environmental Chemistry
07743 Jena (Germany)
E-mail: andrea.balducci@uni-jena.de

[d] D. Carriazo
IKERBASQUE, Basque Foundation for Science
48013 Bilbao (Spain)

 Supporting information for this article is available on the WWW under
<https://doi.org/10.1002/batt.202200508>

 © 2022 The Authors. *Batteries & Supercaps* published by Wiley-VCH GmbH. This is an open access article under the terms of the Creative Commons Attribution Non-Commercial License, which permits use, distribution and reproduction in any medium, provided the original work is properly cited and is not used for commercial purposes.

electrochemical stability. Particularly, hard carbons (HCs) have received great interest due their large specific capacities, low operating potential and excellent cycling performance. Additionally, HCs can be easily obtained from worldwide abundant and easily accessible wastes^[17–19] and their performance as anodes in SiBs generally deliver reversible specific capacities between 200 and 350 mAh g⁻¹ for more than 100 cycles. This behavior is related to the plateau region originated at low voltages, which considerably increases the energy output of the cell.^[20] Moreover, HCs show a similar performance in KiBs, which furtherly demonstrates their great potential as negative electrodes for alkali metal-ion batteries.^[21] Nevertheless, some challenges still need to be issued for the practical application of HCs. Their complex structures comprises abundant defects, edges, functional groups, numerous randomly aligned graphene sheets, pseudo-graphitic microcrystals, and a vast amount of micropores.^[22,23] The precursor selected and the synthetic conditions have a great influence over these parameters, which are of paramount importance for the performance of alkali metal-ion batteries. Thus, the storage of alkali metal ions in hard carbon is very complicated to predict and analyze due to the diverse structures of hard carbon. Moreover, the mechanisms behind insertion/extraction in SiBs and KiBs are still controversial and several confronted arguments can be found in literature.^[21,22,24–26]

So, in this study we investigate the performance of graphene-coffee waste derived hard carbons for the storage of Li, Na and K. Coffee waste was selected as carbonaceous precursor attending to its availability and outstanding performance as anode for LiBs and SiBs.^[27–36] On the other hand, combining HC with other carbonaceous materials is an effective approach to mitigate the inherent disadvantages such as insufficient electrical conductivity. Among them, graphene-based materials are promising candidates due to their ability to create a conductive matrix along the sample.^[37–42] Mechanistic insights of the hybrids HCs are disclosed through electrochemical studies, including GITT, and *operando* XRD.

Experimental

Synthesis

Graphene-coffee waste hard carbon was prepared following the procedure described elsewhere.^[43] Briefly, coffee waste from used capsules of a well-known coffee company and graphene oxide (GO) from GRAPHENE A (4 mg mL⁻¹) were chosen as carbon precursor and graphene source, respectively. In a preliminary step, GO/coffee waste powdered composite was prepared by mixing 2.5 g of coffee waste with 40 mL of 2 mg mL⁻¹ GO and vigorously stirred overnight. Then the suspension was freeze-dried for 3 days to yield the dry GO/coffee waste precursor. Hard carbon graphene composite was obtained by heating the powdered GO/coffee waste mixture at 950 °C for 1 h under dynamic Ar atmosphere. The sample hereafter denoted as rGOCOF was obtained after ball milling (Planetary mill PULVERISETTE 5) at 250 r.p.m. using a carbon:ball mass ratio of 1:30. Milling process (30 minutes) was repeated six times using resting times of 5 minutes between each repetition.

Physicochemical characterization

Morphological characterization was performed by scanning electron microscopy (SEM) in a Quanta200 FEI (3 kV, 30 kV) microscope. Raman spectrum was recorded in a Renishaw spectrometer (Nanometrics Multiview 2000) operating with an excitation wavelength of 532 nm. The spectrum was acquired with 30 s of exposition time of the laser beam to the sample. Nitrogen adsorption/desorption isotherm was registered at -196 °C in an ASAP 2460 from Micromeritics. The specific surface area (SSA) value was calculated from the Brunauer-Emmett-Teller (BET) equation in the relative pressure range between 0.05 and 0.25. The microstructure of the sample was analyzed by X-ray diffraction (XRD) in a Bruker D8 X-ray diffractometer; data were collected using CuK α radiation over 2 θ within the range from 10 to 80° at steps of 0.02°. The interlayer spacing (d_{002}) was calculated according to Bragg's Law:

$$d_{002} = \frac{\gamma}{2 \sin\theta}$$

where θ corresponds to the scattering angle of the C(002) peak position and γ to the copper X-Ray wavelength (1.5406 Å). The crystallite size L_c and L_a were calculated from the Scherrer's formula:

$$L = \frac{K \gamma}{\beta \cos\theta}$$

where K is a shape factor (0.9 and 1.84 for L_c and L_a , respectively) and β is the full width at half maximum (FWHM) of the C(002) and C(100) diffraction peaks for L_c and L_a , respectively.

Electrochemical characterization

Electrodes containing hard carbon were processed by mixing the rGOCOF active material together with Super P C65 (IMERYS Graphite & Carbon) and polyvinylidene fluoride (PVDF) in N-methyl-2-pyrrolidone (NMP) according to the 90:5:5 mass ratio. NMP-based inks were coated on copper and then the laminate was dried at 80 °C under vacuum overnight. Electrode discs of 11 mm in diameter were punched out and dried at 120 °C overnight under vacuum prior the cell assembly. HC-based electrodes were evaluated in a half-cell configuration in a two-electrode Swagelok-type cell and using lithium, sodium or potassium discs as counter and reference electrodes. Whatman D-type glass fibers discs of 13 mm in diameter and a 1 M solution of MTFSI in PC (M: Li, Na or K) were used as separator and electrolyte, respectively. Galvanostatic charge/discharge measurements were carried at different C rates (being 1 C: 372 mAh g⁻¹ according to the theoretical capacity of graphite) between 0.002 and 2.0 V vs. M/M⁺. Cyclic voltammetry measurements were also performed at several scan rates in this potential range. The mobility of the metal ions inside the carbon electrode was investigated using galvanostatic intermittent titration (GITT). In this technique short current impulses are applied to the cell and the voltage response with respect to time is recorded, both during the current impulse and over the relaxation period, when no current is passed. Under the assumption of Fick's second law, the diffusion coefficient obtained after solving the equation^[44] is given by:

$$D = \frac{4}{\pi t} \left(\frac{m_B V_m}{m_B S} \right)^2 \left(\frac{\Delta E_s}{\Delta E_t} \right)^2 (\tau \ll \frac{L^2}{D})$$

Where, m_b is the mass of active material, τ is the relaxation time, V_m is the molar mass of the active material, S is the surface area of the electrode, F is faraday constant, n is number of electron, ΔE_s is the change of steady state voltage at the end of relaxation period and ΔE_t is the total change in cell voltage during current pulse, neglecting ohmic resistance (*IR*) drop. GITT measurements were carried out after 10 activation cycles at 0.1 C. Pulses were performed at 0.1 C with a duration of 20, 15 and 10 min for Li, Na and K cells, respectively. It was established a relaxation time of 2 h between pulses in all the cases. It has to be remarked that since the conditions for the equations are not fulfilled in many real electrodes, a quantitative analysis of the results is not really possible. Nevertheless, as shown^[45,46] the considered model can be used to gain useful and reliable information about the changes of the diffusion coefficient within the investigated potential. Specific capacity and current density values were calculated with respect to the total mass of active material ($1.0 \pm 0.2 \text{ mg cm}^{-2}$). Electrochemical tests were carried out in a VMP3 multichannel potentiostat.

Operando XRD

Operando XRD measurements were performed on a lab-scale Bragg-Brentano diffractometer (Bruker D8 advance, with Cu K- α 1,2 tube source and LYNXEYE 1D detector), using a custom-made in-situ electrochemical cell equipped with Beryllium Windows (see Ref. [47] for more details on the cell design). The 16 mm diameter electrode was prepared by slurry casting the sample onto the Beryllium Window, using the same method than described in section 2.3. The cell was assembled using Whatman D-type glass fibers separator discs of 18 mm impregnated with a 1 M solution of MTFSI in PC (M: Li, Na or K). The cells were then cycled at 0.03 C, and 30 min patterns were collected sequentially with an angular step size of 0.1°. Collected XRD patterns have been corrected by Lorentz-polarization and angular-dependent window absorption as described in reference.^[47]

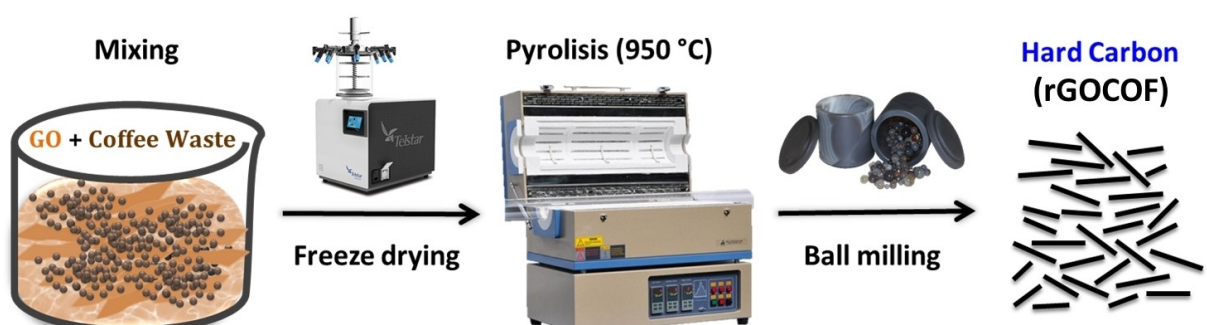
Results and Discussion

As described above, a hard carbon denoted as rGOCOF, was obtained from the pyrolysis of a mixture of GO and coffee waste at 950 °C. As it is widely well known, the carbonization temperature has a strong impact on the graphite interlayer distance, porous structure and number of defects of the synthesized carbon, and thus, on its electrochemical performance for a given alkali metal-ion anode. As previously summarized by Zhao and coworkers,^[21] maximum reversible

specific capacities for LIBs and SIBs are obtained at ca. 900 and 1400 °C, respectively. This should be attributed to the optimum balance between the adsorption capacity undergone on the defect sites and the intercalation capacity that takes place in the pseudo-graphitic domains. In the case of KIBs reversible specific capacities for HC anodes decrease when pyrolysis temperature is increased. Considering the aforementioned arguments, 950 °C was selected as the common temperature for the pyrolysis of the precursors. A further ball milling process was carried out to obtain a homogeneous distribution of carbon particle with a reduced size with the aim of shortening the diffusion pathways of the metallic ions within the carbonaceous electrodes. Moreover, it has been demonstrated that decreasing the carbon particle size led to a larger number of defects and enhanced slope capacities.^[48] This simple, eco-friendly and low-cost synthetic route is summarized in Scheme 1.

SEM images of the coffee waste derived carbon just after its pyrolysis (Figure 1a) show that the material is formed by large millimeter sized particles with a macroporous honeycomb structure. Reduced graphene oxide (rGO) sheets, derived from the thermal reduction of graphene oxide, appear homogeneously covering the surface of the carbon particles providing a conductive network along the whole sample (more detailed information and conductivity measurements can be found in our previous work).^[43] The ball milling treatment results in a significant decrease of the particle size to 2–5 μm as can be observed in Figure 1(b). The reduced particle size along with the rGO-based conductive matrix are expected to fasten the ionic diffusion of the alkaline ions through the carbon particles and increase its electronic conductivity.^[37]

The XRD pattern registered for the rGOCOF (Figure 2a) shows mainly two broad peaks at $2\theta = 24^\circ$ – 26° and $2\theta = 42^\circ$ – 44° . These peaks can be respectively assigned to the C(002) and C(100) reflections between crystal planes of graphitic sheets and the plane of sp²-hybridized hexagonal carbons, respectively. As previously reported, these patterns are characteristic of disordered carbons, such as hard carbons.^[23] According to Bragg's Law the interlayer distance (d_{002}) of rGOCOF corresponds to 3.50 Å, which is slightly higher than the graphene interlayered distance in graphite (3.35 Å). It is worth to remark that the interlayer distance of the graphene-coffee waste hard carbon is slightly lower when compared to other



Scheme 1. Synthetic route followed for the preparation of rGOCOF hard carbon.

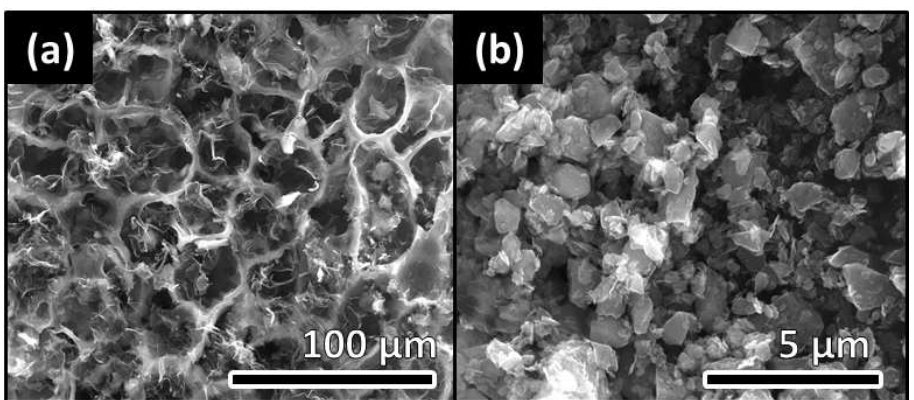


Figure 1. SEM images of graphene-coffee waste hard carbons a) before and b) after the ball milling.

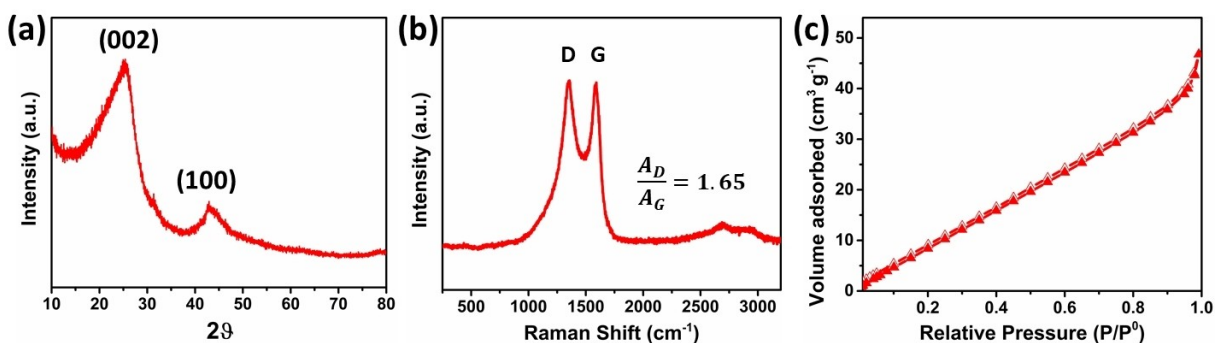


Figure 2. a) XRD pattern, b) Raman spectrum and c) N_2 adsorption/desorption isotherm of rGOCOF sample.

biowaste-derived hard carbons reported in literature which are in the range of 3.7–4.2 Å.^[49] This could be ascribed to the reduction of the disorder degree in the sample due to the addition of graphene as observed in our previous work.^[43] The crystallite size along the *c*-axis (L_c) and the size of the layer planes (L_a) were 13.42 and 64.04 Å, respectively, as calculated by the Scherrer's equation. The Raman spectrum registered for rGOCOF (Figure 2b) shows two broad peaks at *ca.* 1351 and 1599 cm⁻¹, assigned to the G and D bands of carbons, respectively. The G-band is associated to the vibration of sp²-type carbons while the D-band corresponds to the dispersive defect induced vibrations.^[50] Peak intensity ratio of D and G-peaks (I_D/I_G) is a commonly used calculation for the estimation of the disorder degree in carbonaceous structure. However, since D and G-bands show some degree of overlapping, the ratio between peak integrated areas (A_D/A_G) was considered instead. A value of 1.65 is calculated for rGOCOF, indicating the presence of numerous defects in the sample. Textural properties of the sample were assessed by the N_2 adsorption/desorption isotherms registered at –196 °C (Figure 2c). rGOCOF shows a type-III isotherm according to the IUPAC classification,^[51] which corresponds to the adsorption in macroporous or non-porous materials. A specific surface area of only 51 m² g⁻¹ was calculated for this sample, which is in agreement with best performing hard carbons reported in literature for energy storage.^[52] It is important to keep SSA as low as possible to minimize its detrimental effect over coulombic efficiency

evolution, especially in the first cycles due to the appearance of irreversible reactions related to the solid electrolyte interphase (SEI) formation.

To study the electrochemical performance of the graphene-coffee waste derived hard carbons, electrodes were evaluated versus lithium, sodium and potassium in a half-cell configuration. For this purpose, a reference electrolyte system consisting of a 1 M solution of MTFSI in PC (M: Li, Na or K) was used. Galvanostatic charge/discharge curves and corresponding derivatives are included in Figure 3. It can be noted that the galvanostatic profiles recorded during Li⁺, Na⁺ and K⁺ ion insertion/extraction show significant differences from each other. The specific capacity delivered by the Li-based cell (Figure 3a) is mainly contributed from the slopping region as depicted in galvanostatic profiles. In the case of the sodium cell (Figure 3b), two regions can be distinguished at low current densities during sodiation. A slopping region from 2 to *ca.* 0.1 V vs. Na/Na⁺ and a characteristic plateau from 0.1 V vs. Na/Na⁺ until the cutoff potential. It is worth to highlight that the plateau capacity is almost negligible from 0.5 C onwards, as result of the polarization of the cell at high current densities. For the potassium cell (Figure 3c) two distinct regions can be also distinguished but showing a much smoother plateau from *ca.* 0.3 V vs. K/K⁺ until the cutoff potential. Despite the slightly lower interlayer distance measured for rGOCOF (3.50 Å), the galvanostatic profiles registered versus Li, Na and K, resembles other ones previously reported for biowaste derived HCs.^[53]

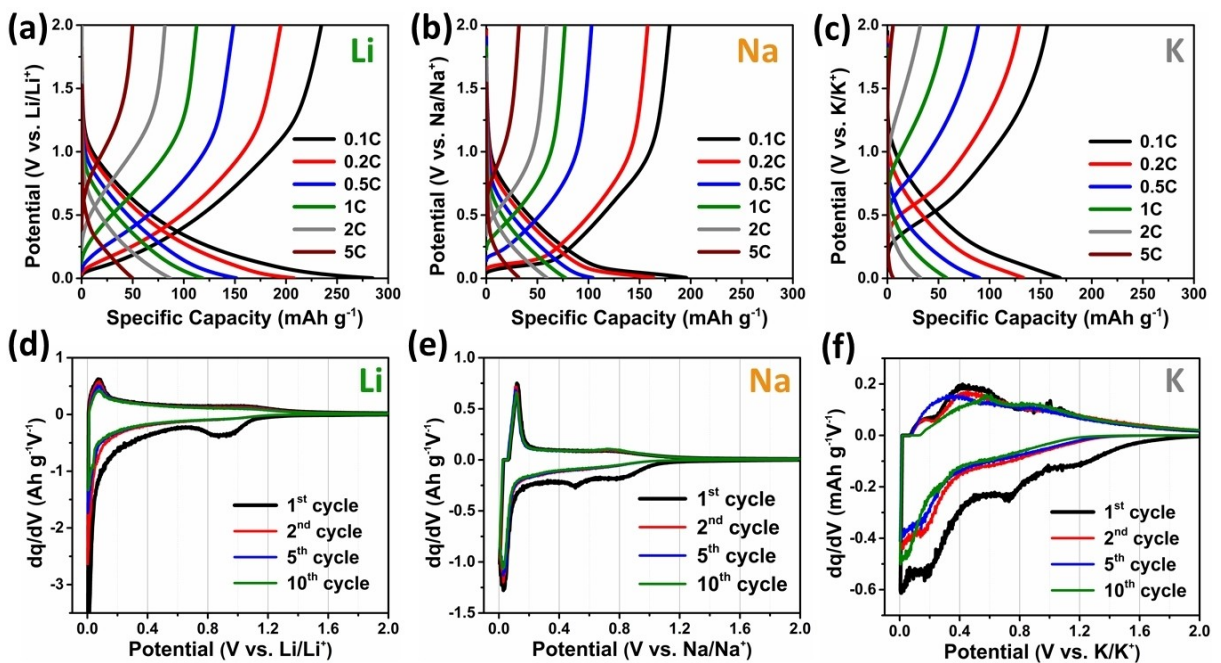


Figure 3. Galvanostatic charge/discharge curves of rGOCOF sample evaluated versus a) lithium, b) sodium and c) potassium, and d-f) corresponding dQ/dV plots.

Differential capacity curves obtained from the first ten cycles at 0.1 C for lithium, sodium and potassium are represented in Figure 3d, e and f, respectively. During the initial discharge, significant current peaks occur at the intervals of 0.7–1.1 V vs. Li/Li⁺ for lithium and 0.4–0.9 V vs. Na/Na⁺ for sodium. In the case of potassium, even if the potential interval cannot be clearly defined due to the wide broadening of the differential capacity in the first cycle, a clear current peak is centered at ca. 0.75 V vs. K/K⁺. This behavior is only detected in the first cycle, and it corresponds to the irreversible decomposition of the electrolyte at the electrode/electrolyte interface and the formation of the SEI. The absence of these current peaks in the next cycles indicates that this SEI is relatively stable.^[2] Nevertheless, coulombic efficiencies (CE) of only 45.1%, 47.7% and 49.2% are obtained in the first cycle at 0.1 C for rGOCOF when measured vs. Li, Na and K, respectively (see Figure S1). Further

optimization of the carbon material and the electrolyte would be necessary to increase the CE of the cells in each of the systems. However, in this particular case and for a shake of comparison, the storage of the three alkaline ions was performed under similar conditions (pyrolysis temperature and type of electrolyte). On the other hand, high intensity peaks are observed in dQ/dV curves at ca. 0 V. It is worth to notice that the insertion/deinsertion potential of these peaks increase with the ionic radius of the evaluated alkaline metal ion (K > Na > Li).^[22]

Significant differences are observed on the specific capacities and capacity retention between the three systems (Figure 4a). Lithium-based cell exhibits larger specific capacity than sodium or potassium counterparts regardless the current density. This behavior contrasts some publications that claimed larger specific capacities in SBs than LIBs when HCs are used as

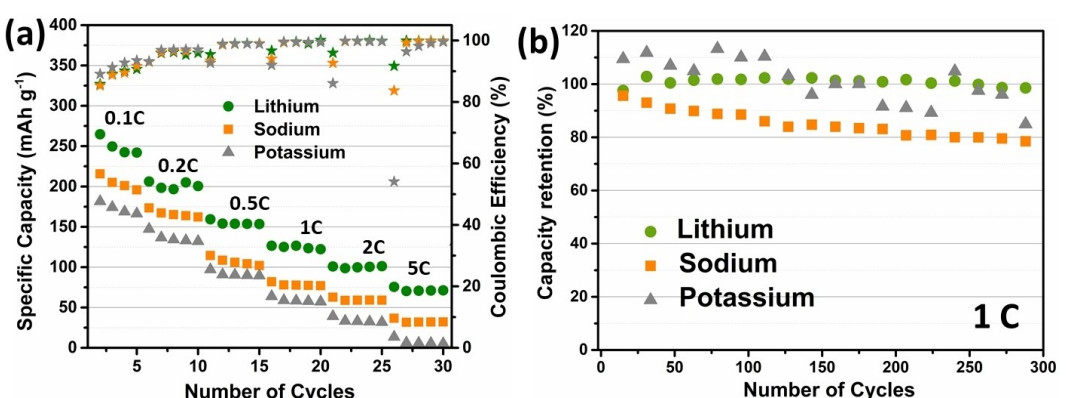


Figure 4. a) C-rate test and b) long-term cyclability studio at 1 C of rGOCOF-based electrodes evaluated versus the noted alkali metals.

anodes.^[25] Specifically, LiB anodes deliver ca. 275 mAh g⁻¹ at 0.1 C and ca. 125 mAh g⁻¹ at 1 C. In the case of sodium, the SiB shows a promising initial specific capacity of ca. 225 mAh g⁻¹ at 0.1 C, but a significant capacity decay takes place when measurements are performed at 0.5 C, which is surely related to the absence of the plateau at low potential at this current density (see Figure 3b). Finally, the potassium cell shows lower specific capacities and capacity retentions in the whole range of current densities. Even if ca. 175 mAh g⁻¹ are attained at 0.1 C, the capacity falls below 50 mAh g⁻¹ from 2 C onwards, which could be ascribed to its lower diffusion kinetics. On this regard, the lithium cell shows a greater capacity retention than Na or K counterparts. This is in good agreement with diffusion coefficient values calculated from cyclic voltammetry measurements (Figure S2, Table S1), where Li-based cell shows the faster diffusion kinetics. A long-term cyclability study of the cells was performed at 1 C for 300 cycles (Figure 4b). The Li-based cell demonstrates an outstanding cycling performance, delivering almost the 100% of the initial capacity after 300 cycles, whereas an 80% is retained for Na and K. However, large capacity fluctuations are observed for the case of potassium, which could be related to the higher reactivity of this element and to its large ionic radius that compromises the stability of the carbonaceous structure upon potassiation/depotassiation. Nevertheless, it is worth noting that a remarkable coulombic efficiency evolution over the 98% after 300 cycles was achieved in all cases (Figure S3).

Operando XRD measurements were performed at 0.03 C versus metallic lithium, sodium and potassium to further investigate the ion storage mechanisms of the HC during charge/discharge. From the patterns registered versus lithium (Figure 5a) it can be clearly observed that upon lithiation the C(002) peak gradually shifts towards smaller diffraction angles while its intensity is progressively decreased. This shift is more pronounced in the voltage range of 1.0–0.15 V vs. Li/Li⁺, confirming the intercalation of the lithium ions in the pseudographitic interlayers in the sloping region.^[54–56] Afterwards, during delithiation the initial peak position and intensity are almost restored, indicating the reversible intercalation/dein-

tercalation of the lithium ions in the HC structure. This unambiguous result contrast with previous publications which argue that the Li⁺ intercalation process does not take place in the sloping region for HCs.^[25,54,57] Thus, the *operando* XRD results suggest that adsorption processes take place at potentials above 1.0 V whereas intercalation of Li⁺ occurs within the sloping region of the LiB. On the other hand, the characteristic low crystallinity of our HC (see Figure 2a) combined with the higher molecular weight of sodium and potassium difficult the interpretation of their XRD patterns. As a consequence, the expected shift of the XRD peaks during sodiation and potassiation is not clearly appreciated in Figure 5(b) and (c), respectively. However, the reversible intercalation of the alkali metal ions in the hard carbon structure is confirmed by the intensity reduction of the peaks upon Na⁺/K⁺ insertion in the electrode.^[58–60] The intensity reduction is more accused for the case of potassium due to its higher atomic number. This intensity change can be clearly appreciated in Figure S4.

In order to extract deeper information about the insertion/extraction mechanisms of Li, Na and K ions in the hosting electrode, GITT measurements were carried out (Figure 6). It should be noted that the ion storage mechanism in hard carbon is strongly related to its microstructure, which is determined by the precursor, the temperature of pyrolysis and the post processing, as well as on the cycling procedure of the electrochemical cell, especially on the current rate and lower cut-off potential. Therefore, general conclusions regarding the storage mechanism undergone in these materials should be treated with caution. The different diffusivities of the Li⁺, Na⁺ and K⁺ ions upon potential change indicate that the insertion/extraction processes vary significantly depending on the alkaline metal ion evaluated. During lithiation, the LiB (Figure 6a) shows a smooth decrease of D_{Li} to ca. 0.1 V vs. Li/Li⁺ which could be ascribed to the either adsorption or intercalation of the Li⁺ on energetically favorable sites.^[25,61] However, while *operando* XRD supports the ion intercalation in the sloping region, GITT measurements does not provide enough information to elucidate if either adsorption or intercalation

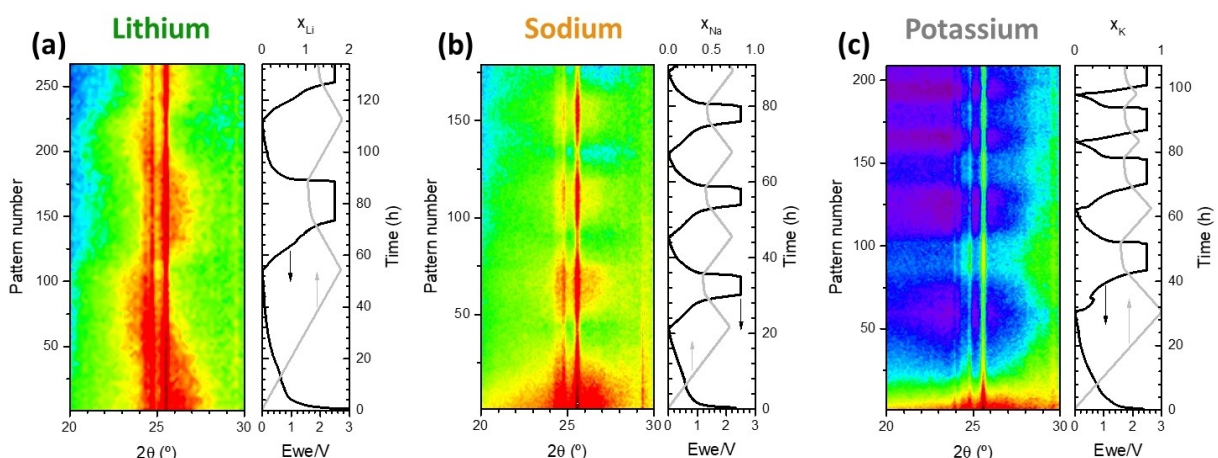


Figure 5. *Operando* XRD measurements of rGOCOF-based HCs versus a) lithium, b) sodium and c) potassium.

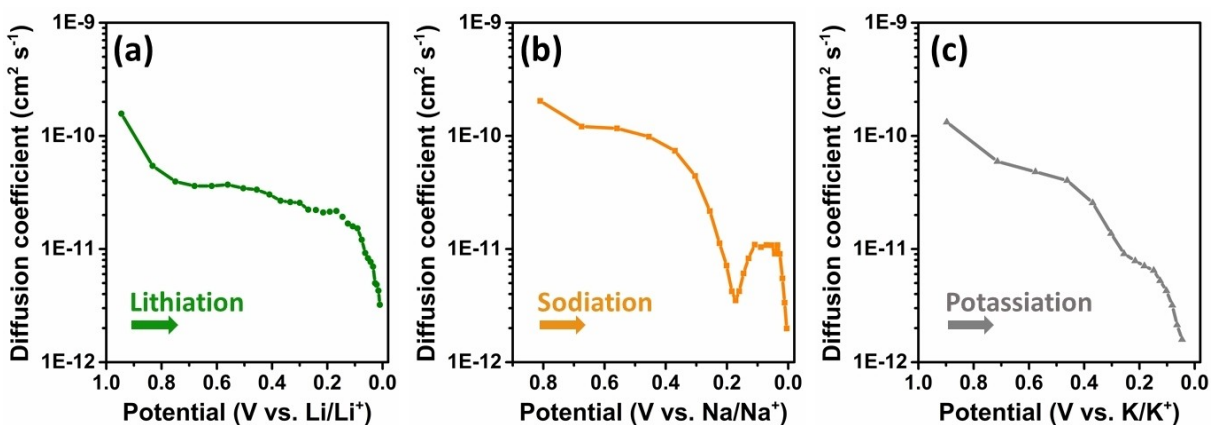


Figure 6. GITT measurements of rGOCOF-based electrodes versus a) lithium, b) sodium and c) potassium.

processes take place in the different regions, and further characterization is needed. From 0.1 V vs. Li/Li⁺ until the cutoff potential, the substantial drop of the diffusion coefficient could be related to the insertion of successive lithium ions on less energetically favorable sites due to the repulsive forces generated by the accumulation of pre-adsorbed ions. For SiB (Figure 6b) a gradual reduction of D_{Na} followed by a fast decline to ca. 0.2 V vs. Na/Na⁺ is observed in the first place. Similar to the LiB, this behavior can be assigned to the adsorption/intercalation of sodium ions. However, unlike in the case of the LiB, D_{Na} shows a rapid increase from ca. 0.2 to 0.1 V vs. Na/Na⁺ followed by an abrupt decrease of D_{Na} until the cutoff potential. This phenomenon taking place in the plateau region of the potential curve (see Figure 3b), may be explained by the filling of Na⁺ in the closed bulk micropores of the HC as greatly reported in literature.^[21,22,55,59,62–65] Finally, for the KIB (Figure 6c), a turnover is not observed like in the case of sodium but it also presents two plateaus. This indicates that different processes are taking place during potassiation in the HC structure, which can be ascribed to adsorption and intercalation mechanisms as demonstrated from the *operando* XRD analysis and in good agreement with recent reports.^[21,24,66] However, it is worth to remark that further studies are needed to elucidate the formation of quasi-metallic metal cluster filling the porous structure of the HC like in the case of SiBs. The GITT curves upon delithiation, desodiation and depotassiation show the exact opposite trend than that observed for the insertion of the alkali metal ions, indicating their reversible desorption from the carbonaceous matrix (see Figure S5).

Conclusion

The potential of a novel hard carbon derived from the pyrolysis of coffee waste and graphene oxide as anode for lithium-ion, sodium-ion and potassium-ion storage has been demonstrated. The electrochemical characterization showed that graphene-coffee waste hard carbon exhibits moderate reversible capacities in all the metals and a good capacity retention of more than 80% of the initial capacity after during 300 charge/

discharge cycles at 1 C regardless the system. Additionally, a comprehensive study performed by *operando* XRD and GITT measurements about the charge storage mechanisms undergone in each of the elements supported that the adsorption of the alkaline metal ions in energetically favorable active sites is produced at the high potential region, while intercalation of ions within the disordered carbon lattice takes place in the sloping region. These results bring additional evidence on the charge storage mechanism undergone in hard carbons.

Acknowledgements

The authors thank the European Union (Graphene Flagship, Core 2, Grant number 785219) and the Spanish Ministry of Science and Innovation (MICINN/FEDER) (RTI2018-096199-B-I00, PID2019-107468RB-C22 and PID2021-127635OB-I00) for the financial support of this work. J.L.G.U. is very thankful to the Spanish Ministry of Education, Science and Universities (MICINN) for the FPU grant (16/03498) and the FPU mobility grant (EST19/00316). S.D.M. C.L. and A.B. thanks the Deutsche Forschungsgemeinschaft (DFG) [project BA4956/21-1] and the Thüringer Ministerium für Wirtschaft, Wissenschaft und Digitale Gesellschaft (TMWWDG) and the Thüringer Aufbau Bank (TAB) within the project LiNaKon (2018 FGR 0092) for financial support. We also want to acknowledge the company GRAPHENEA for supplying the graphene oxide used in this work. Open Access funding enabled and organized by Projekt DEAL.

Conflict of Interest

There are no conflicts to declare

Data Availability Statement

The data that support the findings of this study are available from the corresponding author upon reasonable request.

Keywords: biowaste • graphene • lithium • operando XRD • potassium • sodium

- [1] M. Fleischer, *J. Chem. Educ.* **1954**, *31*, 446.
- [2] Z. Zhu, W. Zhong, Y. Zhang, P. Dong, S. Sun, Y. Zhang, X. Li, *Carbon Energy* **2021**, *3*, 541–553.
- [3] C. Vaalma, D. Buchholz, M. Weil, S. Passerini, *Nat. Rev. Mater.* **2018**, *3*, 18013.
- [4] I. Hasa, D. Buchholz, S. Passerini, J. Hassoun, *ACS Appl. Mater. Interfaces* **2015**, *7*, 5206–5212.
- [5] W. Li, Z. Bi, W. Zhang, J. Wang, R. Rajagopalan, Q. Wang, D. Zhang, Z. Li, H. Wang, B. Wang, *J. Mater. Chem. A* **2021**, *9*, 8221–8247.
- [6] P. Barpanda, L. Lander, S. Nishimura, A. Yamada, *Adv. Energy Mater.* **2018**, *8*, 1703055.
- [7] T. Hosaka, T. Shimamura, K. Kubota, S. Komaba, *Chem. Rec.* **2019**, *19*, 735–745.
- [8] X. Yin, S. Sarkar, S. Shi, Q. Huang, H. Zhao, L. Yan, Y. Zhao, J. Zhang, *Adv. Funct. Mater.* **2020**, *30*, 1908445.
- [9] W. Zhang, W. Huang, Q. Zhang, *Chem. Eur. J.* **2021**, *27*, 6131–6144.
- [10] P. Ge, M. Fouletier, *Solid State Ionics* **1988**, *28*, 1172–1175.
- [11] Y. Liu, B. V. Merinov, W. A. Goddard, *Proc. Natl. Acad. Sci.* **2016**, *113*, 3735–3739.
- [12] H. Moriwake, A. Kuwabara, C. A. J. Fisher, Y. Ikuhara, *RSC Adv.* **2017**, *7*, 36550–36554.
- [13] Y. Li, Y. Lu, P. Adelhelm, M.-M. Titirici, Y.-S. Hu, *Chem. Soc. Rev.* **2019**, *48*, 4655–4687.
- [14] K. Song, C. Liu, L. Mi, S. Chou, W. Chen, C. Shen, *Small* **2021**, *17*, 1903194.
- [15] Y. Wu, C. Zhang, H. Zhao, Y. Lei, *J. Mater. Chem. A* **2021**, *9*, 9506–9534.
- [16] Z. Hong, H. Maleki, T. Ludwig, Y. Zhen, M. Wilhelm, D. Lee, K.-H. Kim, S. Mathur, *J. Energy Chem.* **2021**, *62*, 660–691.
- [17] K. Hong, L. Qie, R. Zeng, Z. Yi, W. Zhang, D. Wang, W. Yin, C. Wu, Q. Fan, W. Zhang, Y. Huang, *J. Mater. Chem. A* **2014**, *2*, 12733.
- [18] T. Zhang, J. Mao, X. Liu, M. Xuan, K. Bi, X. L. Zhang, J. Hu, J. Fan, S. Chen, G. Shao, *RSC Adv.* **2017**, *7*, 41504–41511.
- [19] C. Nita, B. Zhang, J. Dentzer, C. Matei Ghimeau, *J. Energy Chem.* **2021**, *58*, 207–218.
- [20] M. Thompson, Q. Xia, Z. Hu, X. S. Zhao, *Mater. Adv.* **2021**, *2*, 5881–5905.
- [21] L. Zhao, Z. Hu, W. Lai, Y. Tao, J. Peng, Z. Miao, Y. Wang, S. Chou, H. Liu, S. Dou, *Adv. Energy Mater.* **2021**, *11*, 2002704.
- [22] Y. Huang, Y. Wang, P. Bai, Y. Xu, *ACS Appl. Mater. Interfaces* **2021**, *13*, 38441–38449.
- [23] X. Dou, I. Hasa, D. Saurel, C. Vaalma, L. Wu, D. Buchholz, D. Bresser, K. Shinichi, S. Passerini, *Mater. Today* **2019**, *23*, 87–104.
- [24] C. Chen, M. Wu, Y. Wang, K. Zaghib, *J. Power Sources* **2019**, *444*, 227310.
- [25] S. Alvin, H. S. Cahyadi, J. Hwang, W. Chang, S. K. Kwak, J. Kim, *Adv. Energy Mater.* **2020**, *10*, 2000283.
- [26] D. Saurel, B. Orayech, B. Xiao, D. Carriazo, X. Li, T. Rojo, *Adv. Energy Mater.* **2018**, *8*, 1703268.
- [27] F. Luna-Lama, D. Rodríguez-Padrón, A. R. Puente-Santiago, M. J. Muñoz-Batista, A. Caballero, A. M. Balu, A. A. Romero, R. Luque, *J. Cleaner Prod.* **2019**, *207*, 411–417.
- [28] S. J. Hong, S. S. Kim, S. Nam, *Corros. Sci. Technol.* **2021**, *20*, 15–21.
- [29] M. E. Lee, H. W. Kwak, H.-J. Jin, Y. S. Yun, *ACS Sustainable Chem. Eng.* **2019**, *7*, 12734–12740.
- [30] H. Darjazi, A. Staffolani, L. Sbrascini, L. Bottone, R. Tossici, F. Nobili, *Energies* **2020**, *13*, 6216.
- [31] G. Gao, L.-Z. Cheong, D. Wang, C. Shen, *Carbon Resour. Convers.* **2018**, *1*, 104–108.
- [32] Y. J. Hwang, S. K. Jeong, K. S. Nahm, J. S. Shin, A. Manuel Stephan, *J. Phys. Chem. Solids* **2007**, *68*, 182–188.
- [33] P.-H. Chiang, S.-F. Liu, Y.-H. Hung, H. Tseng, C.-H. Guo, H.-Y. Chen, *Energy Fuels* **2020**, *34*, 7666–7675.
- [34] J. H. Um, Y. Kim, C.-Y. Ahn, J. Kim, Y.-E. Sung, Y.-H. Cho, S.-S. Kim, W.-S. Yoon, *J. Electrochem. Sci. Technol.* **2018**, *9*, 163–168.
- [35] Q. Xie, S. Qu, Y. Zhang, P. Zhao, *Appl. Surf. Sci.* **2021**, *537*, 148092.
- [36] S.-Y. Tsai, R. Muruganantham, S.-H. Tai, B. K. Chang, S.-C. Wu, Y.-L. Chueh, W.-R. Liu, *J. Inst. Chem.* **2019**, *97*, 178–188.
- [37] W. Luo, C. Bommier, Z. Jian, X. Li, R. Carter, S. Vail, Y. Lu, J.-J. Lee, X. Ji, *ACS Appl. Mater. Interfaces* **2015**, *7*, 2626–2631.
- [38] G. Yasin, M. Arif, T. Mehab, M. Shakeel, M. A. Mushtaq, A. Kumar, T. A. Nguyen, Y. Slimani, M. T. Nazir, H. Song, *Inorg. Chem. Front.* **2020**, *7*, 402–410.
- [39] G. Jialin, P. Zheng, *Appl. Phys. A* **2021**, *127*, 509.
- [40] J. L. Gómez-Urbano, G. Moreno-Fernández, M. Granados-Moreno, T. Rojo, D. Carriazo, *Batteries & Supercaps* **2021**, *4*, 1749–1756.
- [41] J. L. Gómez-Urbano, M. Entería, I. Monterrubio, I. Ruiz de Larramendi, D. Carriazo, N. Ortiz Vitoriano, T. Rojo, *ChemSusChem* **2020**, *13*, 1203–1225.
- [42] G. Moreno-Fernández, M. Granados-Moreno, J. L. Gómez-Urbano, D. Carriazo, *Batteries & Supercaps* **2021**, *4*, 469–478.
- [43] J. L. Gómez-Urbano, G. Moreno-Fernández, M. Arnaiz, J. Ajuria, T. Rojo, D. Carriazo, *Carbon* **2020**, *162*, 273–282.
- [44] W. Weppner, R. A. Huggins, *J. Electrochem. Soc.* **1977**, *124*, 1569–1578.
- [45] M. Schroeder, S. Menne, J. Ségalini, D. Saurel, M. Casas-Cabanas, S. Passerini, M. Winter, A. Baldacci, *J. Power Sources* **2014**, *266*, 250–258.
- [46] C. Leibing, A. Baldacci, *J. Electrochem. Soc.* **2021**, *168*, 090533.
- [47] D. Saurel, A. Pendasheth, M. Jáuregui, M. Reynaud, M. Fehse, M. Galceran, M. Casas-Cabanas, *Chemistry-Methods* **2021**, *1*, 248–248.
- [48] H. Lu, F. Ai, Y. Jia, C. Tang, X. Zhang, Y. Huang, H. Yang, Y. Cao, *Small* **2018**, *14*, 1802694.
- [49] U. Mittal, L. Djuandhi, N. Sharma, H. L. Andersen, *J. Phys. Energy* **2022**, *4*, 042001.
- [50] J.-B. Wu, M.-L. Lin, X. Cong, H.-N. Liu, P.-H. Tan, *Chem. Soc. Rev.* **2018**, *47*, 1822–1873.
- [51] M. Thommes, K. Kaneko, A. V. Neimark, J. P. Olivier, F. Rodriguez-Reinoso, J. Rouquerol, K. S. W. Sing, *Pure Appl. Chem.* **2015**, *87*, 1051–1069.
- [52] P. Yu, W. Tang, F.-F. Wu, C. Zhang, H.-Y. Luo, H. Liu, Z.-G. Wang, *Rare Met.* **2020**, *39*, 1019–1033.
- [53] S. Darlam-Magar, C. Leibing, J. L. Gómez-Urbano, D. Carriazo, A. Baldacci, *Energy Technol.* **2022**, *10*, 2200379.
- [54] R. Muruganantham, F.-M. Wang, R. A. Yuwono, M. Sabugaa, W.-R. Liu, *Energy Fuels* **2021**, *35*, 10878–10889.
- [55] D. A. Stevens, J. R. Dahn, *J. Electrochem. Soc.* **2001**, *148*, A803.
- [56] S. Komaba, W. Murata, T. Ishikawa, N. Yabuchi, T. Ozeki, T. Nakayama, A. Ogata, K. Gotoh, K. Fujiwara, *Adv. Funct. Mater.* **2011**, *21*, 3859–3867.
- [57] S. Qiu, L. Xiao, M. L. Sushko, K. S. Han, Y. Shao, M. Yan, X. Liang, L. Mai, J. Feng, Y. Cao, X. Ai, H. Yang, J. Liu, *Adv. Energy Mater.* **2017**, *7*, 1700403.
- [58] B. Zhang, C. M. Ghimeau, C. Laberty, C. Vix-Guterl, J.-M. Tarascon, *Adv. Energy Mater.* **2016**, *6*, 1501588.
- [59] Y. Morikawa, S. Nishimura, R. Hashimoto, M. Ohnuma, A. Yamada, *Adv. Energy Mater.* **2020**, *10*, 1903176.
- [60] K. Zhang, Q. He, F. Xiong, J. Zhou, Y. Zhao, L. Mai, L. Zhang, *Nano Energy* **2020**, *77*, 105018.
- [61] L. Xie, C. Tang, Z. Bi, M. Song, Y. Fan, C. Yan, X. Li, F. Su, Q. Zhang, C. Chen, *Adv. Energy Mater.* **2021**, *11*, 2101650.
- [62] K. Kubota, S. Shimadzu, N. Yabuchi, S. Tominaka, S. Shiraishi, M. Abreu-Sepulveda, A. Manivannan, K. Gotoh, M. Fukunishi, M. Dahbi, S. Komaba, *Chem. Mater.* **2020**, *32*, 2961–2977.
- [63] C. Bommier, T. W. Surta, M. Dolgos, X. Ji, *Nano Lett.* **2015**, *15*, 5888–5892.
- [64] M. Dahbi, M. Kiso, K. Kubota, T. Horiba, T. Chafik, K. Hida, T. Matsuyama, S. Komaba, *J. Mater. Chem. A* **2017**, *5*, 9917–9928.
- [65] N. Zhang, Q. Liu, W. Chen, M. Wan, X. Li, L. Wang, L. Xue, W. Zhang, *J. Power Sources* **2018**, *378*, 331–337.
- [66] R. C. Cui, B. Xu, H. J. Dong, C. C. Yang, Q. Jiang, *Adv. Sci.* **2020**, *7*, 1902547.

Manuscript received: November 24, 2022

Revised manuscript received: December 21, 2022

Accepted manuscript online: December 23, 2022

Version of record online: January 9, 2023